JOURNAL OF GEOPHYSICAL RESEARCH, VOL. ???, XXXX, DOI:10.1029/,

# A Wall-like Sharp Downward Branch of the Walker Circulation above the Western Indian Ocean

Tsubasa Kohyama[1], Tamaki Suematsu[2], Hiroaki Miura[3], and Daisuke Takasuka[1]

Key points:

- Climatology and interannual variability of the zonally-thin downward branch above the Indian Ocean are discussed.
- Model experiments confirm that the sharp downward branch is sustained by East African topography, in addition to radiative cooling.
- Without mountains in East Africa, the eastern Horn of Africa would exhibit wetter and more convective climatology.

---

Corresponding author: T. Kohyama, Department of Information Sciences, Ochanomizu University, 2-1-1, Otsuka, Bunkyo-ku, Tokyo, 112-8610, Japan. (tsubasa@is.ocha.ac.jp)

[1]Department of Information Sciences, Ochanomizu University, Tokyo, Japan.

[2]Atmosphere and Ocean Research Institute, The University of Tokyo, Tokyo, Japan.

[3]Department of Earth and Planetary Science, The University of Tokyo, Tokyo, Japan.

**Abstract.** In the zonal direction, the downward branch of the Walker circulation above the Indian Ocean is only 20 degrees thick, whereas the Pacific counterpart is 90 degrees thick. This zonal sharpness is remarkable because atmospheric disturbances smaller than the planetary scale, such as the Asian Summer Monsoon, can interact with the planetary-scale Walker circulation through this branch. As a moist circulation, this zonal sharpness is imprinted on a unique zonal discontinuity of the Intertropical Convergence Zone, which has direct implications for the dry climate in the Northeast Africa. Therefore, in this study, we refer to this zonally-thin downward branch as the "Wall", investigate its climatology and interannual variability, and aim at determining its reason for existence.

The strongest season of the lower tropospheric Wall in boreal summer is sustained by horizontal cold advection associated with the Asian Summer Monsoon. Two weak phases of the Wall correspond to two rainy seasons at the Eastern Horn of Africa, which are not reproduced well by state-of-the-art global climate models. As to interannual variability, a mass-weighted vertical mean of vertical motion at the Wall exhibits a tight linkage to the tropical Pacific, though total variance is explained more by local sea surface temperature.

Model experiments using a convection-permitting atmospheric general circulation model show that mountains in East Africa are necessary for the existence of the Wall. Vertical mixings forced by mountain waves play a fundamental role in strengthening the Wall. After flattening the East African

topography, zonal discontinuity of the Intertropical Convergence Zone disappears.

## 1. Introduction

The Walker circulation is the most prominent planetary-scale tropical atmospheric circulation in the zonal direction [e.g., *Walker*, 1923, 1924; *Bjerknes*, 1969]. It has been understood that, to first order, the vertical motion associated with the Walker circulation consists of upward branches over relatively warm surface (e.g., the warm pool in the western Pacific) and downward branches over relatively cool surface (e.g., the cold tongue in the eastern Pacific) [e.g., *Lau and Yang*, 2003]. In the context of climate variability, the Pacific branches of the Walker circulation have received particular attention, because its interannual fluctuation serves as the atmospheric component of the El Niño Southern Oscillation, the most dominant interannual climate mode on Earth [e.g., *Bjerknes*, 1969].

As a mean state, however, a downward branch of the Walker circulation above the western Indian Ocean also exhibits a strong subsidence, which is at least comparable to the Pacific downward branch. Figure 1a shows the annual-mean equatorial vertical motion calculated by taking the meridional mean over the equatorial region (10°S-10°N). The strong and sharp downward branch stands at the western edge of the Indian Ocean (40°E-60°E), whereas the weak and wide downward branch lies over the eastern Pacific (90°W-150°W). Considering the size of the two oceanic basins, one might find this interbasin contrast counterintuitive.

In fact, the interbasin difference in apparent strength of the downward motion emanates from a minor cause. An important caveat of this meridional-mean view shown in Fig. 1a is that the strength of the downward motion depends upon latitudinal choices of the equatorial belt. Figure 2a shows the annual-mean meridional-mean equatorial vertical motion over the equatorial belt of 10°S-10°N, 5°S-5°N, and 2°S-2°N. While the downward branch above the Indian Ocean relatively keeps its strength notwithstanding the latitudinal choices, that of the eastern Pacific becomes stronger when narrower equatorial belts are chosen. A key to understand this difference is the zonal-mean crosssection (Fig. 2b). The outstanding difference between the Indian and the Pacific downward branches is the degree of meridional asymmetry. The apparent weak downward motion above the Pacific, shown in Fig. 1a, originates from an offset of a strong upward branch over the northern off-equatorial region (4°N-10°N) against a strong equatorial downward motion over 10°S-2°N. On the other hand, the downward branch above the Indian Ocean shown in Fig. 1a consists of a strong downward branch over 4°S-10°N with a hint of weak upward branch located to the south. Though it could be misleading in some context, we will carefully keep using the equatorial belt of 10°S-10°N in this study, because we are interested in the meridionally-broad equatorial downward branch above the Indian Ocean.

A more fundamental difference between the two downward branches lies in the zonal thickness. That is, the downward branch above the Indian Ocean is only 20 degrees thick in the zonal direction, whereas the Pacific counterpart is about 90 degrees thick. As we shall see in later sections, this zonal sharpness of the Indian Ocean branch is remarkable in the sense that phenomena smaller than the planetary scale, such as the Asian Summer Monsoon and possibly mountain waves, can easily interact with the planetary-scale Walker circulation via this branch. This zonal sharpness is particularly notable in the lower tropospheric layer, where the downward branch subsides only onto the coastal western Indian Ocean and not onto the African continent (Fig. 2c), which is consistent with *Yang et al.* [2015]. In addition, from the viewpoint of moist circulations, the zonally-thin downward branch is imprinted on a unique zonal discontinuity of the Intertropical Convergence Zone (ITCZ). Figures 1b and 1c show the annual mean outgoing longwave radiation (OLR) and precipitation, respectively, over the tropics. ITCZ is typically characterized by the narrow convective band that circles the Earth along the equatorial region, but if we carefully look at ITCZ, a discontinuity of ITCZ is found at the western edge of the Indian Ocean.

One of major implications of this ITCZ discontinuity, and thereby, of the zonally-thin downward branch, is the relatively dry climate at the so-called "Eastern Horn of Africa", whose mean state, annual cycle, variability, and change have long been investigated in many previous studies [e.g., *Camberlin*, 1995; *Schreck III and Semazzi*, 2004; *Liebmann et al.*, 2014; *Lyon*, 2014; *Tierney et al.*, 2015; *Liebmann et al.*, 2017]. By investigating the zonally-thin downward branch, we expect a better understanding of the climatology at the Eastern Horn of Africa, whose annual cycle of precipitation is poorly reproduced by state-of-the-art global climate models [*Tierney et al.*, 2015].

Therefore, in this study, we refer to this meridionally-broad, zonally-thin sharp downward branch above the Indian Ocean as the "Wall" of the Walker Circulation, and will investigate its climatology and interannual variability in the hope that its reason for existence will be determined. Data and methods are described in the next section. In section 3, we describe the seasonality of the Wall, and highlight a role of horizontal cold advection to support its strongest phase. Next, in section 4, we define the Wall index to describe the interannual variability of the Wall and point out that both remote and local SST explain the interannual variance. In section 5, we then perform model experiments to identify the East African topography as a necessary condition for the existence of the

Wall, and discuss implications for the climate at the Eastern Horn of Africa. Conclusions are presented in section 6.

## 2. Data and Model

### 2.1. Data

Observed vertical motion, wind, and temperature data are from the European Center for Medium range Weather Forecasting (ECMWF) ERA-Interim reanalysis data [*Dee et al.*, 2011], and the time span used in this study is from 1979 through 2017. Observed OLR data is from the National Oceanic and Atmospheric Administration (NOAA) interpolated OLR [*Liebmann and Smith*, 1996], whose time span used in this study is from June 1974 through December 2018. Observed precipitation data is from the Global Precipitation Climatology Project (GPCP) [*Adler et al.*, 2003], and the time span used in this study is from January 1979 through January 2020. The horizontal resolutions used in this study are 3° for vertical motion, wind, and temperature, and 2.5° for OLR and precipitation.

### 2.2. Atmospheric General Circulation Model (AGCM) experiments

We use the Nonhydrostatic Icosahedral Atmospheric Model (NICAM) [*Tomita and Satoh*, 2004; *Satoh et al.*, 2008, 2014], the version of which used for our experiments is the latest stable version, NICAM16-S [*Kodama et al.*, 2020]. The condensation processes are explicitly calculated using the single moment water 6 microphysics scheme [*Tomita*, 2008a]. Sub-grid scale turbulence is calculated by a modified version of the Mellor-Yamada scheme [*Mellor and Yamada*, 1982; *Nakanishi and Niino*, 2004; *Noda et al.*, 2010]. The radiation model with two stream radiative transfer scheme employs a correlated $k$-distribution method (mstrnX) [*Sekiguchi and Nakajima*, 2008]. Surface fluxes are calculated with a modified version of the Louis scheme [*Louis*, 1979; *Uno et al.*, 1995]. For the land processes, the minimal advanced treatments of surface interaction and runoff (MATSIRO) land model [*Takata et al.*, 2003] is used. Orographic gravity wave drag is considered to be sufficiently resolved in our simulations and to be opted out of employing the parameterization for the sub-grid scale orographic gravity wave drag.

The horizontal resolution is approximately 14 km on an icosahedral hexagonal-pentagonal mesh [*Tomita*, 2008b]. A terrain following vertical grid coordinate is employed with the model top of approximately 40 km and 38 vertical layers, whose thickness increases with height. The model time step is 60 seconds. Our simulations are initialized on 00 UTC 28 June 2013, 2015, and 2016, and are integrated for 93 days for each year. Initial conditions of the atmosphere and the ocean are derived from the National Centers for Environmental Prediction (NCEP) Final Operational Model Global Tropospheric Analysis (NCEP-FNL) [*NCEP*, 2015]. Time evolution of the sea surface temperature is prescribed externally from the interpolation of the NCEP-FNL data at 00 UTC on each day. To mitigate the effect of the model bias over land, the initial conditions of the land surface are taken from the monthly climatology derived from the last 5 years of a 10-year simulation of NICAM at 220 km horizontal resolution following *Kodama et al.* [2015, 2020].

Because it takes approximately 45 days for the values of vertical motions to converge to realistic climatological values, the first 63 days of the integrations are taken as a spin-up period, and the last 30 days of the integrations starting from 1 September are analyzed in this study. For comparison, we have also performed the same simulation but initialized on 00 UTC 28 April 2016 to capture the strongest month of the Wall, i.e., July. Climatology of the Walker circulation, however, is not reproduced well, presumably because the observed downward branches are not established until the end of May, during which the integration cannot be used as a spin-up period to capture the target circulation. Though the AGCM used in this study realistically simulates the mean field over long time periods, the reproducibility of quick variations within relatively short time scales, such as a transition of seasons, is insufficient, to which future improvement is needed.

## 3. Climatology of the Wall

In this section, we first overview the seasonality of the Wall and the consistency with the local rainy seasons. Then, from the energetic viewpoint, we show that the strongest phase of the Wall is supported by horizontal cold advection associated with the Asian Summer Monsoon.

### 3.1. Two-peak seasonality of the Wall

The Wall exhibits two-peak seasonal variability in its strength of the subsidence. The left panels of Fig. 3 shows the monthly climatological-mean equatorial vertical motion averaged over the base period of 1979-2017. The Wall exhibits moderate subsidence from January through March, almost disappears from April through May, reaches its strongest phase from June through September, and becomes weak from October through December.

The phase of this two-peak seasonality corresponds well to the annual precipitation cycle of the Eastern Horn of Africa, where two rainy seasons are known to exist. In this region, the term "Long Rains" denotes the longest and wettest rainy season that lasts from March through May, and the term "Short Rains" denotes the shorter and drier rainy season that peaks in October. Presumably, the lack of this seasonality in state-of-the-art GCMs [*Tierney et al.*, 2015] is inseparable from the reproducibility of the seasonal variability of the Wall.

### 3.2. Role of horizontal cold advection for building the rigid Wall in its strongest phase

One of the essential features of the strongest phase of the Wall is that the subsidence reaches the surface, which is not the case in weaker phases (Fig. 3). In the Wall, horizontal temperature advection plays a key role for lower tropospheric atmospheric subsidence to extend to the surface. The right panels of Fig. 3 shows the mean horizontal temperature advection, which is defined as the inner product of climatological horizontal wind and the horizontal gradient of climatological temperature. Our definition of the mean horizontal advection does not take eddy heat transport into account.

The strongest subsidence observed in the lower troposphere from June through September is supported by the mean horizontal advection. In general, adiabatic heating of large-scale downward motions is needed to balance radiative cooling in the tropics, and this energy budget is mostly true for the Walker circulation as well [*Veiga et al.*, 2011]. As described in the previous paragraph, however, it is not the case for the Wall. The contribution from the horizontal cold advection makes this "subsidence extension" be a distinctive feature that can be observed particularly in the strong phases of the Wall.

The horizontal cold advection is tightly connected to the Asian Summer Monsoon. The top panels of Fig. 4 shows vertical-mean views of the horizontal temperature advection decomposed into zonal and meridional components. The horizontal advection cools the Wall region in boreal summer, when the Wall reaches its maximum phase (Fig. 4, top left). This horizontal advection is realized by the meridional advection (Fig. 4, top right), rather than the zonal component (Fig. 4, top middle). In the bottom panels of Fig. 4, these components are further decomposed into zonal wind, zonal temperature gradient, meridional wind, and meridional temperature gradient. Based on these panels, the maximum horizontal advection in boreal summer originates from the southerly winds associated with Asian Summer Monsoon, which blows toward the upgradient direction of the temperature field in this season.

Presumably, the aforementioned cooling effect drags down the lower tropospheric Walker Circulation to the surface, which is capable of strengthening the downward flow of the Wall further. This notion is consistent with the disappearance of the Wall from April through May, because this season is the period when the Asian summer monsoon are weakened to switch its direction before the onset of the strong Somali jet in early June [e.g., *Findlater*, 1969]. From an energetic viewpoint, the relevance of the Somali jet is also consistent with *Heaviside and Czaja* [2013], who showed that the Somali jet dominantly accomplishes the atmospheric cross-equatorial heat transport.

## 4. Interannual variability of the Wall

In this section, we define the Wall index to point out that both remote and local sea surface temperature (SST) variability explains the interannual variations of the Wall.

### 4.1. Definition of the Wall index

To highlight the interannual variability of the Wall, we define the Wall index as the average over vertical motions at 250, 550, and 850 hPa. This index should be physically interpreted as the mass-weighted average of vertical motions for the upper (100-400 hPa), middle (400-700 hPa), and lower (700-1000 hPa) tropospheric layers. Figure 5a shows that, to first order, the downward motion for the interannual scale is vertically constant, which justifies the definition of the Wall index for the purpose of representing the downward motion throughout the troposphere.

### 4.2. Relationship with ENSO and local SST variability

The interannual variability of the Wall is explained by the El Niño Southern Oscillation (ENSO), which reminds us of the notion that the Wall is a part of the Walker circulation. Figure 5b shows the 5-month running-meaned timeseries of the Wall index. Also shown is the 5-month running-meaned Niño 3.4 index, which is defined as SST anomalies averaged over the Niño 3.4 region (5°S-5°N, 170°W-120°W), but the sign is reversed. These two indices exhibits a correlation of 0.54 (1982-2017), which is significant at the 95% confidence level. During an El Niño event, the Wall region exhibits a weakly downward motion, and vice versa for a La Niña event. In particular, the strong negative peaks of the Wall index in 1982, 1997, and 2015 are well-explained by big El Niño events, whereas the strong positive peaks of the Wall index in 1998, 2010, and 2016 are well-explained by big La Niña events.

The association with ENSO is also verified by SST spatial patterns. Figure 5c shows the regression map of SST anomalies on the Wall index. This map clearly shows that the Wall variability is projected onto the equatorial Pacific SST variability. Because interannual variance of the tropical SST variability in the Pacific is dominated by ENSO, it is virtually certain that ENSO is one of the key factors to understand the Wall climate variability.

That being said, the clear regression pattern in the Pacific does not necessarily mean that the Wall variance is predominantly explained by ENSO. Figure 5d shows the same map as Fig. 5c but for correlation coefficients. Based on this correlation map, though

ENSO still retains its importance, local SST variability in the western equatorial Indian Ocean explains more variance of the Wall. Also notable is the high positive correlations over the maritime continent, presumably because the strength of the upward motions allowed in this region is also inseparable from the amount of the downward motions realized in the whole tropics, following the continuity equation.

## 5. Role of the East African topography for sustaining the Wall

Though we have concluded in section 3 that strong subsidence in the lower troposphere is associated with horizontal temperature advection, it remains unexplored what makes the subsidence in the Wall so strong that the Wall penetrates the entire troposphere in the vertical direction. In particular, cooling mechanisms of the upper troposphere has been largely unexplored. Therefore, in this section, we perform model experiments to highlight the role of topography for sustaining the Wall. Some implications for the climate of the Eastern Horn of Africa are also discussed.

### 5.1. Model experiments with flat East African topography

Our experiments are inspired by *Naiman et al.* [2017], who showed, in an interesting way, that topography can play major roles in determining the tropical circulation. Using the Geophysical Fluid Dynamics Laboratory (GFDL)-Earth System Model (ESM) 2M, they performed an experiment called "Pancake", in which they removed all the topography on Earth and simulated the air-sea coupled system with flat lands. Because the Wall disappears in their "Pancake" run, we have hypothesized that, by flattening topography regionally rather than globally, it is possible to pinpoint the location of mountains that directly contribute to the realization of the Wall. In this regard, *Ogwang et al.* [2014]

also investigated a precipitation response to regionally flattened African topography and demonstrated that the mean rainfall significantly reduces at the west of the Wall region. Based on their results, the hydrology at the center of the Wall may be also modulated.

In this study, in addition to a control run, an AGCM experiment is arranged where the East African topography is regionally flattened. The experiment is named "Flat East Africa (FEA)", in which the elevations are set to be 1 meter over the entire East African region (30°S-30°N, 30°E-50°E) (Fig. 6a). The top and middle panels of Fig. 6b shows the monthly-mean equatorial vertical motion in September 2013 (ENSO neutral) and 2016 (La Niña) based on observations and the control experiment, respectively. The control runs in both years simulates the observed vertical motion associated with the Walker circulation well, so it is justified to investigate the Wall using this AGCM. We have also performed the same experimental sets but for 2015, an El Niño year, but the control run does not reproduce the observed features of the Walker circulation. This poor reproducibility of the Wall during an El Niño year appears to be because the observed Wall is weaker than those of other years (Fig. 5b). In our model, the water vapor supply from the anomalously warm eastern equatorial Pacific is biased to be excessive. The Walker Circulation over the tropics is distorted by this bias, to which the zonally-thin downward branch is sensitive. Therefore, for the rest of this article, only the ENSO neutral and La Niña years will be discussed.

The FEA experiment reveals that, without the East African topography, the Wall disappears almost entirely through the troposphere (Fig. 6b, bottom). By comparing the control and FEA runs, at least in both 2013 and 2016, the East African topography is a necessary condition for the exsistence of the Wall.

A promising hypothesis is that the lack of turbulence generated by mountain waves suppresses vertical mixings. Because the lower troposphere generally has lower potential temperature than the upper troposphere, the reduction of vertical heat exchange weakens the subsidence of upper tropospheric air. Figure 7a shows the difference of equatorial vertical motions between the control and FEA runs, which should be interpreted as the downward motion forced by the East African topography. In this model, the downward branch is shifted west compared to observations, so 30°E-45°E is drawn. Also shown in the left panel of Fig. 7b is the energetic tendency contributions by the sum of eddy heat transport (EHT) and longwave radiation. Here, the EHT contribution is calculated as follows.

$$\mathrm{EHT} = -\frac{\partial \overline{u'T'}}{\partial x} - \frac{\partial \overline{v'T'}}{\partial y} - \frac{\partial \overline{w'T'}}{\partial z} \tag{1}$$

where $x$, $y$, and $z$ denotes zonal, meridional, and vertical coordinates, respectively; $u$, $v$, and $w$ denotes zonal wind, meridional wind, and vertical motion, respectively; $T$ denotes temperature. The overlines denote the mean over September simulated in the model, and the primes denote deviations from the mean.

EHT and longwave radiation explain how East African topography works for realizing the vertical motion. In particular, the downward motion at higher levels than 10 km is predominantly explained by the eddy heat transport (Fig. 7b, middle). The phase of heat and momentum transport is shifted, which suggests a hint of stationary gravity waves forced by mountains. Because the mountain waves suppress the upper tropospheric cloudiness, radiative cooling is enhanced in the middle tropospheric layer (Fig. 7b, right), which in turn strengthens the downward motion further.

A caveat of this heat budget analysis is that the cooling effects of eddy transport and longwave radiation is quantitatively insufficient to explain the total downward motion. By assuming the dry adiabatic lapse rate, the vertical motion of 500 m/day requires approximately 5 °C/day of cooling, but the aforementioned effects only explains 1 °C/day of cooling. Though more dominant effect may exist, it is still hard to close perfectly the heat budget based on an analysis of the 6-hourly snapshots. Nevertheless, by using the convection permitting model without artificial gravity wave drags, our experiments at least confirm that decent amount of the upper tropospheric downward motion is sustained by eddy heat transport forced by East African topography, rather than radiative cooling. Radiative cooling, enhanced by the clearer condition, is only capable of contributing the downward motion in lower altitudes where specific humidity is higher.

This vertical mixing effect serves as a good example where interscale interaction plays a fundamental role in downward branches, in addition to convective upward branches, to realize the large-scale atmospheric circulation in the current tropical climate. Specifically, the narrowly localized downward branch above the western Indian Ocean is realized with a help of interactions between large-scale motions and disturbances in smaller horizontal scales than the weak temperature gradient approximation [*Sobel et al.*, 2001].

### 5.2. Implications for the climate of the Eastern Horn of Africa

Without the East African topography, the relatively dry climate at the Eastern Horn of Africa would become wetter than in the real world. Figure 8 shows the monthly-mean OLR and precipitation near the Wall in 2013 and 2016. The control run of the high-resolution convection-permitting model reproduces both OLR and precipitation well, particularly the discontinuity of ITCZ. In the FEA run, as the East African topography is flattened, the discontinuity of ITCZ disappears, which makes the Eastern Horn of Africa be covered by ITCZ. Our result is consistent with a model experiment without topography performed by *Chou and Neelin* [2003], which does not exhibit the ITCZ discontinuity.

Both local processes and remote forcings can contribute to the "closing" of the ITCZ discontinuity in the FEA run. Locally, the removal of the Wall enhances convection above the Eastern Horn of Africa. This enhancement is due to the reduction of large-scale atmospheric subsidence as discussed in the last subsection. In addition to this local instability effect, clouds and moist air, which are advected remotely by zonal winds, are also allowed to enter the Eastern Horn of Africa from the interior of the African continent, because topographic obstacles do not exist.

## 6. Summary and Discussions

We have reconsidered the climatology and the interannual variability of the Walker circulation by focusing on its sharp downward branch, which we refer to as the Wall, observed at the western edge of the Indian Ocean (Figs. 1 and 2). A distinctive feature of the Wall is the two-peak seasonality (Fig. 3). The two weak phases of the Wall, one in boreal spring and the other in boreal fall, correspond well to the two rainy seasons at the Eastern Horn of Africa, which is not reproduced well by state-of-the-art GCMs. Another distinctive feature is that the subsidence of the Wall in its strongest phase reaches the surface (Fig. 1a). This "subsidence extension" appears to be sustained by horizontal cold advection associated with the Asian Summer Monsoon (Figs. 3 and 4). The interannual variability of the Walker circulation is in no doubt associated with ENSO, but more variance is explained by SSTs in western equatorial Indian Ocean and over the maritime continent (Fig. 5).

AGCM experiments show that the East African topography determines the strength of the Wall (Fig. 6). In the FEA experiment, where the East African mountains are broadly flattened, the Wall almost vanishes throughout the entire tropospheric layer. This result leads to a conclusion that the East African topography is necessary for the existence of the Wall. We hypothesize that the role of topography is to generate mountain waves in response to large-scale circulation. The stationary vertical mixings enhance vertical heat exchange to cool the upper troposphere, which makes the Wall rigid (Fig. 7). Assuming this mechanism, climate variability of the Wall could also be understood based on interscale interactions between macroscopic large-scale circulation and microscopic mountain waves. In addition, based on *Chakraborty et al.* [2009], we could also hypothesize that the modulation of the Somali jet strength by the African topography could control the lower tropospheric downward motion. Our simulation, however, does not reproduce the lower tropospheric downward motion realistically enough to make a case for the role of horizontal advection. Further process studies are needed to improve the robustness of these physical processes.

An implication of our conclusion is that the dry and clear climate at the Eastern Horn of Africa is sustained by the East African topography (Fig. 8). As a local effect, the large-scale subsidence associated with the Wall suppresses the local convection by drying the environment and by suppressing upward motion. At the same time, the high mountains in the East Africa serves as obstacles that prevents clouds and moist air from being conveyed from the interior of the African continent. Because both of these local and remote processes are consistent with the essentiality of the East African topography, it remains to be an open question which process serves as the dominant cause of the ITCZ discontinuity.

**Acknowledgments.** This study is based on the ERA-Interim dataset available online at `https://apps.ecmwf.int/datasets/data/interim-full-moda/levtype=pl/`, the NOAA interpolated OLR dataset available online at `https://psl.noaa.gov/data/gridded/data.interp_OLR.html`, and the GPCP dataset available online at `https://psl.noaa.gov/data/gridded/data.gpcp.html`. The first author is supported by the Japan Society for the Promotion of Science (JSPS)-Kakenhi Grant Number 19K23460 and 20K14554. The third author is supported by JSPS-Kakenhi Grant Number 16H04048. The fourth author is supported by JSPS-Kakenhi Grant Number 20J00605. The numerical computations using NICAM is performed on a super computer, Oakforest-PACS.

## References

Adler, R. F., G. J. Huffman, A. Chang, R. Ferraro, P.-P. Xie, J. Janowiak, B. Rudolf, U. Schneider, S. Curtis, D. Bolvin, et al. (2003), The version-2 global precipitation climatology project (gpcp) monthly precipitation analysis (1979–present), *J. Hydrometeor.*, *4*(6), 1147–1167.

Bjerknes, J. (1969), Atmospheric teleconnections from the equatorial Pacific, *Mon. Wea. Rev.*, *97*(3), 163–172.

Camberlin, P. (1995), June-september rainfall in north-eastern Africa and atmospheric signals over the tropics: A zonal perspective, *International Journal of Climatology*, *15*(7), 773–783.

Chakraborty, A., R. S. Nanjundiah, and J. Srinivasan (2009), Impact of African orography and the Indian summer monsoon on the low-level Somali jet, *Int. J. Climatol.*, *29*(7), 983–992.

Chou, C., and J. D. Neelin (2003), Mechanisms limiting the northward extent of the northern summer monsoons over North America, Asia, and Africa, *J. Climate*, *16*(3), 406–425.

Dee, D. P., S. M. Uppala, A. Simmons, P. Berrisford, P. Poli, S. Kobayashi, U. Andrae, M. Balmaseda, G. Balsamo, d. P. Bauer, et al. (2011), The ERA-Interim reanalysis: Configuration and performance of the data assimilation system, *Quart. J. Roy. Meteor. Soc.*, *137*(656), 553–597.

Findlater, J. (1969), A major low-level air current near the Indian Ocean during the northern summer, *Quarterly Journal of the Royal Meteorological Society*, *95*(404), 362–380.

Heaviside, C., and A. Czaja (2013), Deconstructing the Hadley cell heat transport, *Quart. J. Roy. Meteor. Soc.*, *139*(677), 2181–2189.

Kodama, C., Y. Yamada, A. T. Noda, K. Kikuchi, Y. Kajikawa, T. Nasuno, T. Tomita, T. Yamaura, H. G. Takahashi, M. Hara, et al. (2015), A 20-year climatology of a NICAM AMIP-type simulation, *Journal of the Meteorological Society of Japan. Ser. II*, *93*(4), 393–424.

Kodama, C., T. Ohno, T. Seiki, H. Yashiro, A. T. Noda, M. Nakano, Y. Yamada, W. Roh, M. Satoh, T. Nitta, D. Goto, H. Miura, T. Nasuno, T. Miyakawa, Y.-W. Chen, and M. Sugi (2020), The non-hydrostatic global atmospheric model for cmip6 highresmip simulations (nicam16-s): Experimental design, model description, and sensitivity experiments, *Geoscientific Model Development Discussions*, *2020*, 1–50, doi: 10.5194/gmd-2019-369.

Lau, K., and S. Yang (2003), Walker circulation, *Encyclopedia of atmospheric sciences*, pp. 2505–2510.

Liebmann, B., and C. A. Smith (1996), Description of a complete (interpolated) outgoing longwave radiation dataset, *Bull. Amer. Meteor. Soc.*, *77*(6), 1275–1277.

Liebmann, B., M. P. Hoerling, C. Funk, I. Bladé, R. M. Dole, D. Allured, X. Quan, P. Pegion, and J. K. Eischeid (2014), Understanding recent eastern Horn of Africa rainfall variability and change, *Journal of Climate*, *27*(23), 8630–8645.

Liebmann, B., I. Bladé, C. Funk, D. Allured, X.-W. Quan, M. Hoerling, A. Hoell, P. Peterson, and W. M. Thiaw (2017), Climatology and interannual variability of boreal spring wet season precipitation in the eastern horn of africa and implications for its recent decline, *Journal of Climate*, *30*(10), 3867–3886.

Louis, J.-F. (1979), A parametric model of vertical eddy fluxes in the atmosphere, *Boundary-Layer Meteorology*, *17*(2), 187–202.

Lyon, B. (2014), Seasonal drought in the Greater Horn of Africa and its recent increase during the March–May long rains, *Journal of Climate*, *27*(21), 7953–7975.

Mellor, G. L., and T. Yamada (1982), Development of a turbulence closure model for geophysical fluid problems, *Reviews of Geophysics*, *20*(4), 851–875.

Naiman, Z., P. J. Goodman, J. P. Krasting, S. L. Malyshev, J. L. Russell, R. J. Stouffer, and A. T. Wittenberg (2017), Impact of mountains on tropical circulation in two Earth system models, *Journal of Climate*, *30*(11), 4149–4163.

Nakanishi, M., and H. Niino (2004), An improved Mellor–Yamada level-3 model with condensation physics: Its design and verification, *Boundary-layer meteorology*, *112*(1), 1–31.

NCEP (2015), NCEP GDAS/FNL 0.25 degree global tropospheric analyses and forecast grids.

Noda, A. T., K. Oouchi, M. Satoh, H. Tomita, S.-i. Iga, and Y. Tsushima (2010), Importance of the subgrid-scale turbulent moist process: Cloud distribution in global cloud-resolving simulations, *Atmospheric Research*, *96*(2-3), 208–217.

Ogwang, B. A., H. Chen, X. Li, and C. Gao (2014), The influence of topography on East African October to December climate: sensitivity experiments with RegCM4, *Adv. Meteor.*, *2014*.

Satoh, M., T. Matsuno, H. Tomita, H. Miura, T. Nasuno, and S.-i. Iga (2008), Nonhydrostatic icosahedral atmospheric model (NICAM) for global cloud resolving simulations, *Journal of Computational Physics*, *227*(7), 3486–3514.

Satoh, M., H. Tomita, H. Yashiro, H. Miura, C. Kodama, T. Seiki, A. T. Noda, Y. Yamada, D. Goto, M. Sawada, et al. (2014), The non-hydrostatic icosahedral atmospheric model: Description and development, *Progress in Earth and Planetary Science*, *1*(1), 18.

Schreck III, C. J., and F. H. Semazzi (2004), Variability of the recent climate of eastern Africa, *International Journal of Climatology: A Journal of the Royal Meteorological Society*, *24*(6), 681–701.

Sekiguchi, M., and T. Nakajima (2008), A k-distribution-based radiation code and its computational optimization for an atmospheric general circulation model, *Journal of Quantitative Spectroscopy and Radiative Transfer*, *109*(17-18), 2779–2793.

Sobel, A. H., J. Nilsson, and L. M. Polvani (2001), The weak temperature gradient approximation and balanced tropical moisture waves, *J. Atmos. Sci.*, *58*(23), 3650–3665.

Takata, K., S. Emori, and T. Watanabe (2003), Development of the minimal advanced treatments of surface interaction and runoff, *Global and planetary Change*, *38*(1-2), 209–222.

Tierney, J. E., C. C. Ummenhofer, and P. B. deMenocal (2015), Past and future rainfall in the Horn of Africa, *Sci. Adv.*, *1*(9), e1500,682.

Tomita, H. (2008a), New microphysical schemes with five and six categories by diagnostic generation of cloud ice, *Journal of the Meteorological Society of Japan. Ser. II*, *86*, 121–142.

Tomita, H. (2008b), A stretched icosahedral grid by a new grid transformation, *Journal of the Meteorological Society of Japan. Ser. II*, *86*, 107–119.

Tomita, H., and M. Satoh (2004), A new dynamical framework of nonhydrostatic global model using the icosahedral grid, *Fluid Dynamics Research*, *34*(6), 357.

Uno, I., X.-M. Cai, D. Steyn, and S. Emori (1995), A simple extension of the Louis method for rough surface layer modelling, *Boundary-layer meteorology*, *76*(4), 395–409.

Veiga, J. A. P., V. B. Rao, and S. H. Franchito (2011), Annual mean analysis of the tropical heat balance and associations with the Walker circulation, *Revista Brasileira de Meteorologia*, *26*(1), 01–08.

Walker, G. T. (1923), Correlations in seasonal variation of weather, VIII: A preliminary study of world weather, *Mem. Indian Meteorol. Dep.*, *24*, 75–131.

Walker, G. T. (1924), Correlations in seasonal variations of weather, IX: A further study of world weather, *Mem. Indian Meteorol. Dep.*, *24*, 275–332.

Yang, W., R. Seager, M. A. Cane, and B. Lyon (2015), The annual cycle of East African precipitation, *J. Climate*, *28*(6), 2385–2404.

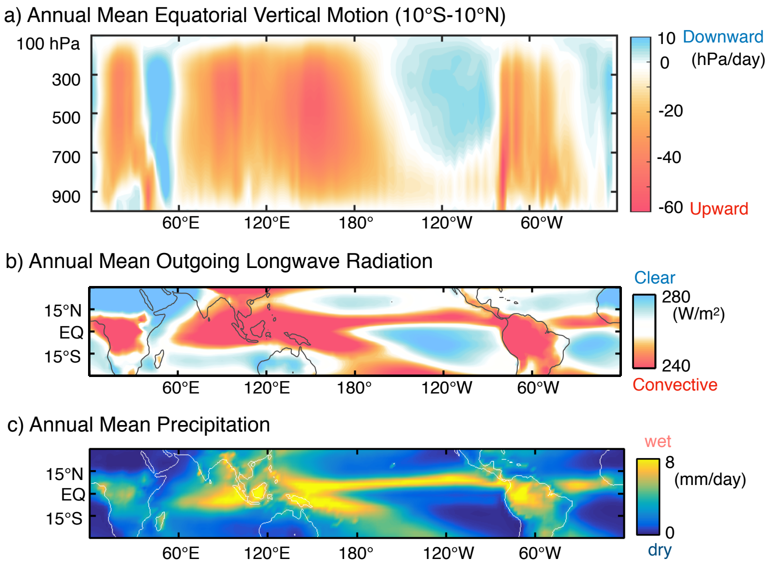


**Figure 1.** (a): Observed annual-mean vertical motion averaged meridionally over the equatorial region (10°S-10°N). (b): Observed annual-mean outgoing longwave radiation (OLR). (c): Observed annual-mean precipitation.

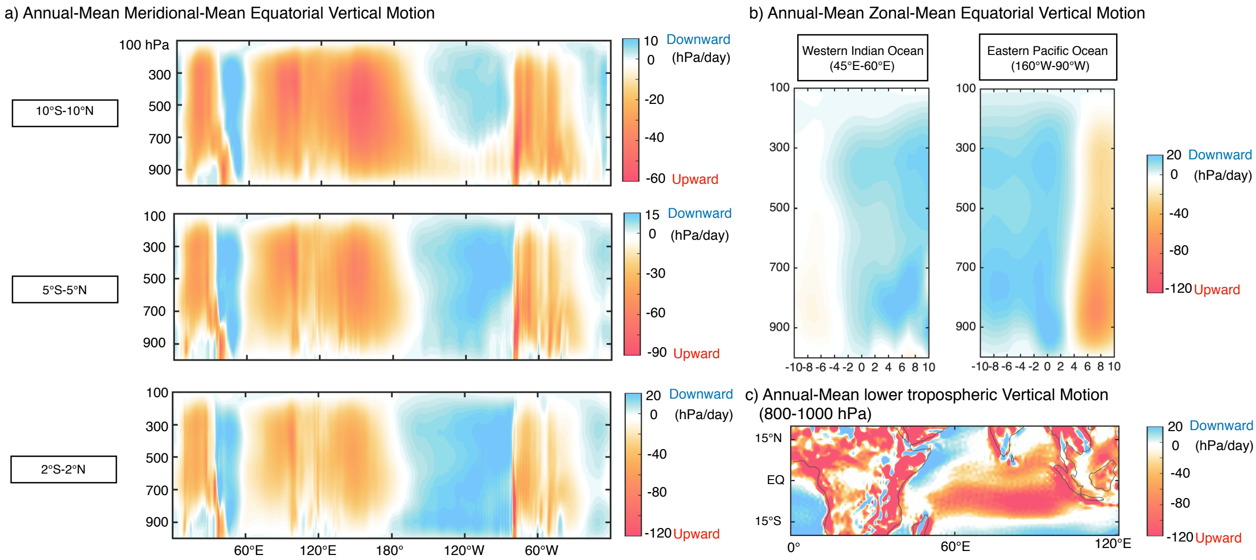


**Figure 2.** (a): As in Fig. 1a, but over the equatorial belt of 10°S-10°N (top) , 5°S-5°N (middle), and 2°S-2°N (bottom). (b): As in Fig. 1a, but averaged zonally over the Western Indian Ocean (45°E-60°E) and the Eastern Pacific Ocean (160°W-90°W). (c): As in Fig. 1a, but averaged vertically over the lower troposphere (800-1000hPa).

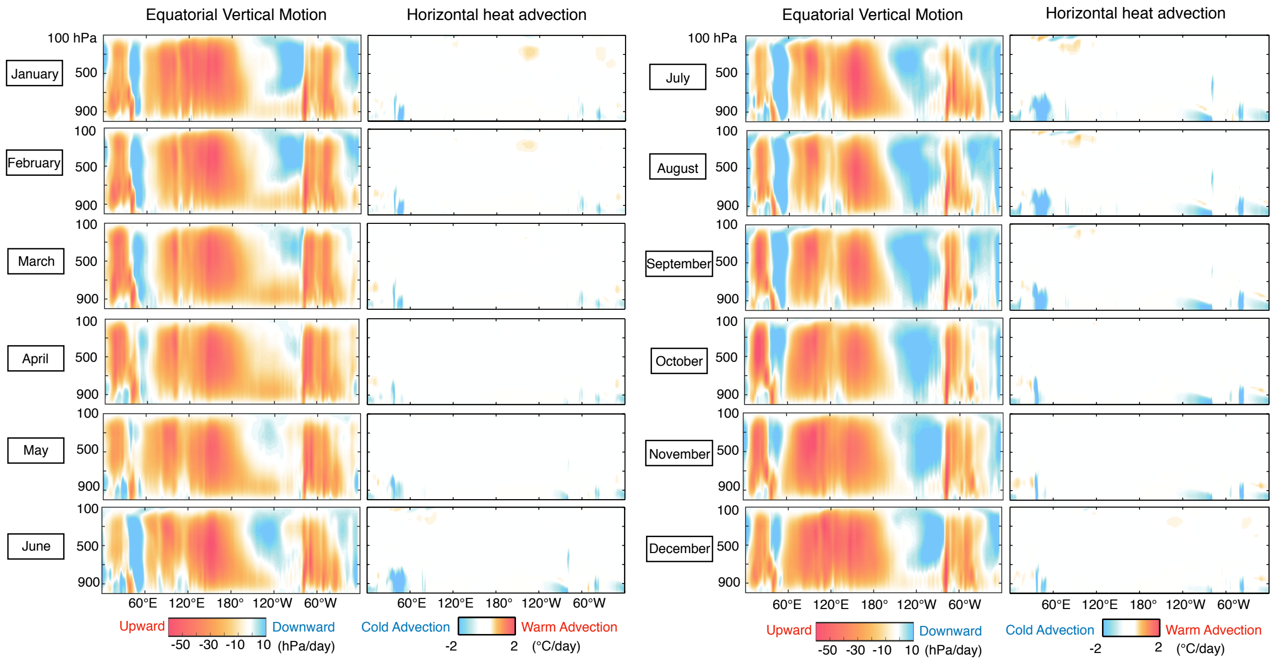


**Figure 3.** Left columns, As in Fig. 1a, but monthly mean values for each month averaged over 1979-2017. Right columns, As in right, but for mean horizontal advection defined as the inner product of mean horizontal wind and the horizontal gradient of mean temperature.

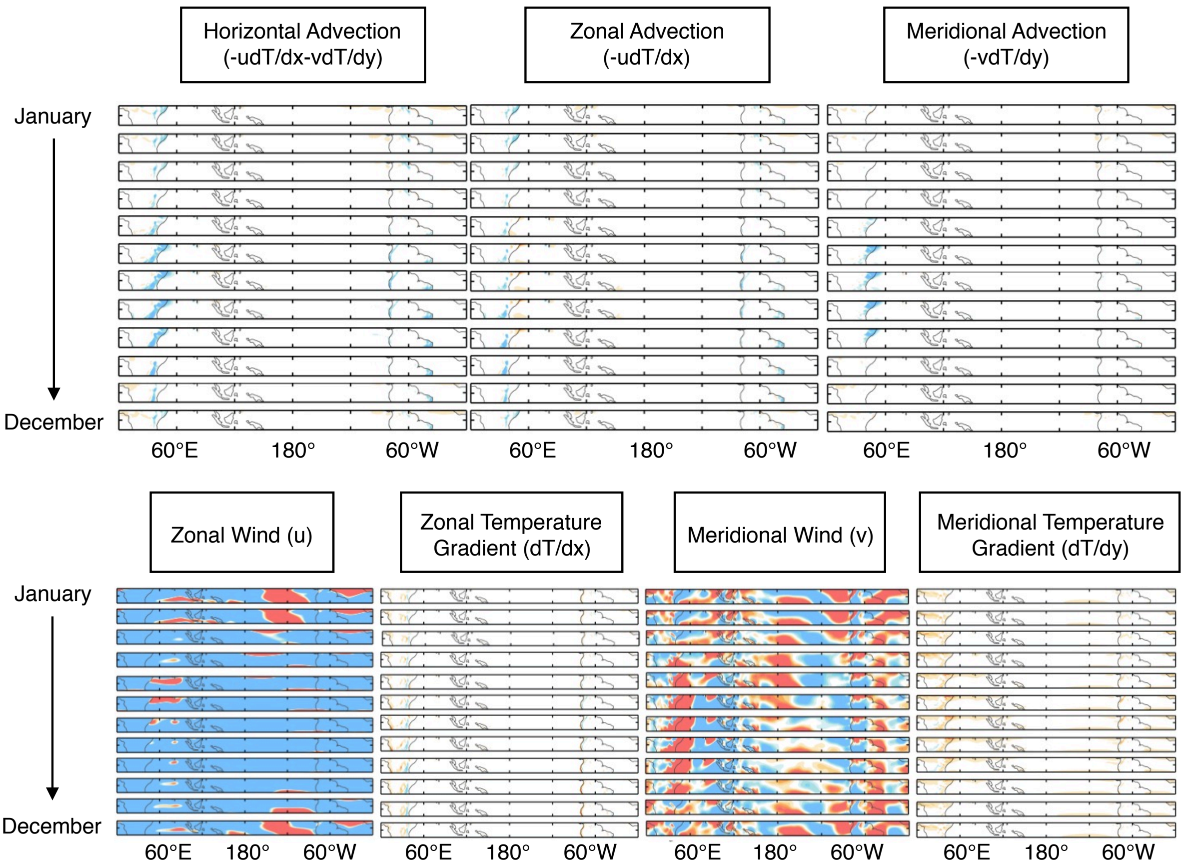


**Figure 4.** Top, As in the right columns of Fig. 3, but for vertical-mean tropospheric horizontal advection (left), zonal advection (middle), and meridional advection (right). Contribution of eddy transport is not considered. Bottom, As in top, but for zonal wind (left), zonal temperature gradient (second from the left), meridional wind (second from the right), and meridional temperature gradient (right).

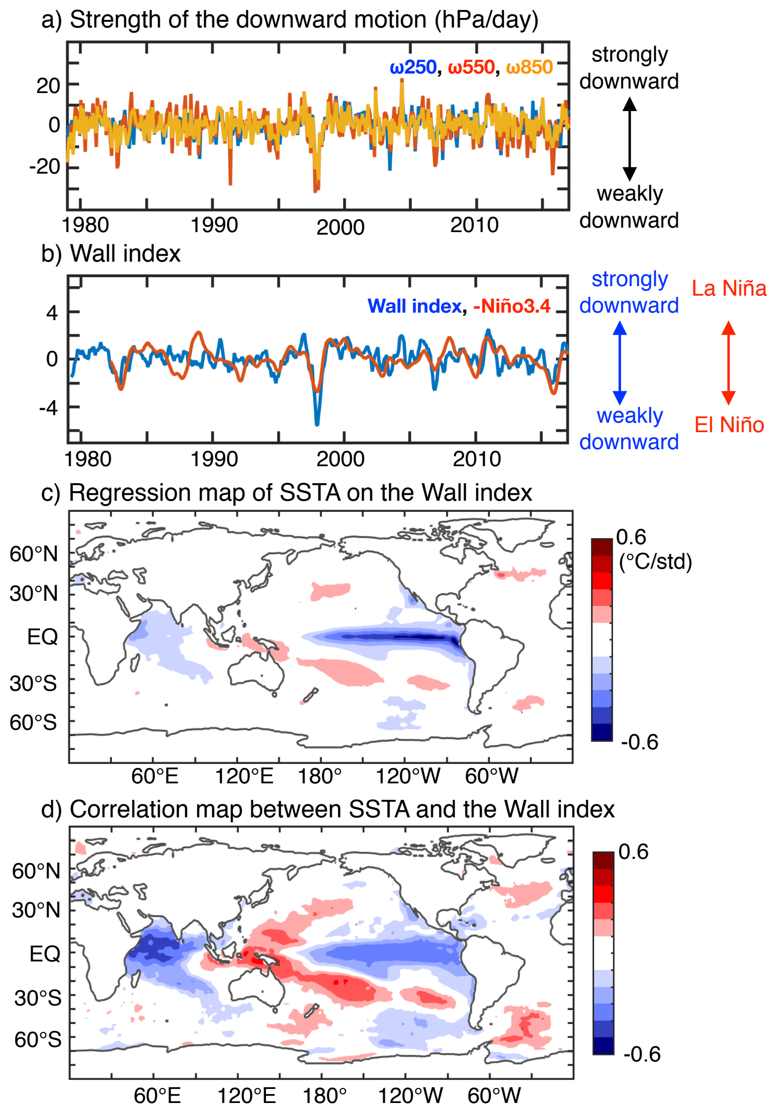


**Figure 5.** (a): Time series of the observed monthly-mean vertical motion at 250 hPa (blue), 550 hPa (red), and 850 hPa (yellow), averaged over the Wall region (10°S-10°N, 40°E-60°E). (b): Blue, Time series of the Wall index defined as the mean of the three time series shown in (a) standardized by its own standard deviation. Red, Niño 3.4 index defined as the regional-mean sea surface temperature anomalies (SSTA) over the Niño 3.4 region (5°S-5°N, 170°W-120°W) standardized by its own standard deviation and the sign is reversed. (c): Regression map of SSTA on the Wall index. (d) Correlation map between SSTA and the Wall index.

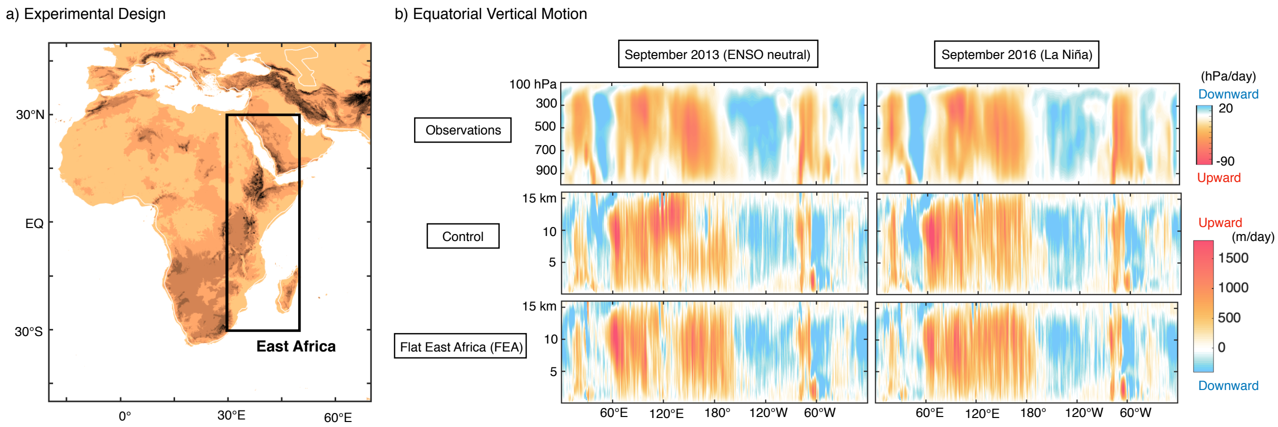


**Figure 6.** (a): Topography of the entire African continent. Black box shows the East African region (30°S-30°N, 30°E-50°E). (b): As in Fig. 1a, but for one-month mean values calculated for September 2013 (left) and 2016 (right) based on observations, the control, and the Flat East Africa (FEA) experiment in this order from the top panel. In the FEA experiment, the topography in the East African region, shown as the black box in (a), is flattened and set to be 1 meter.

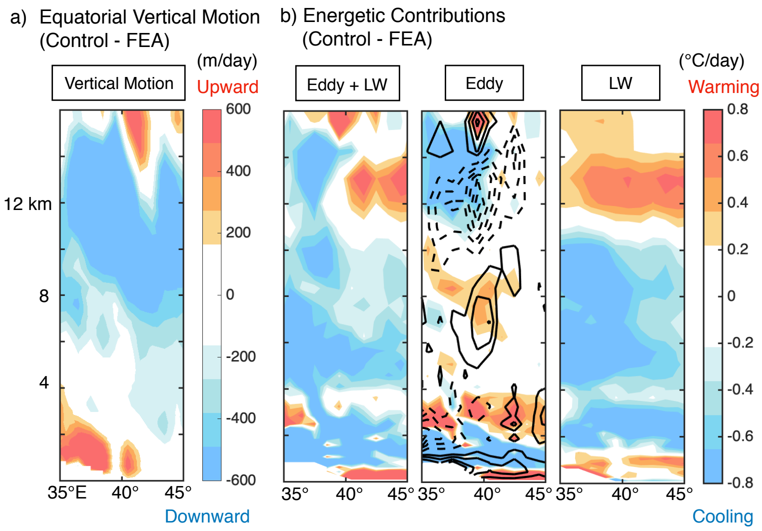


**Figure 7.** (a): As in the right panel of Fig. 6b, but the difference between the control and FEA runs in 35°E-45°E. (b): As in (a), but the energetic tendency contributions by the sum of eddy heat transport and longwave radiation (left), eddy heat transport (middle), and longwave radiation (right). Also shown as contours in the middle panel is eddy vertical momentum transport. Solid (dashed) curves denote upward (downward) vertical momentum transport. Contour interval is 0.05 (m/s)/day.

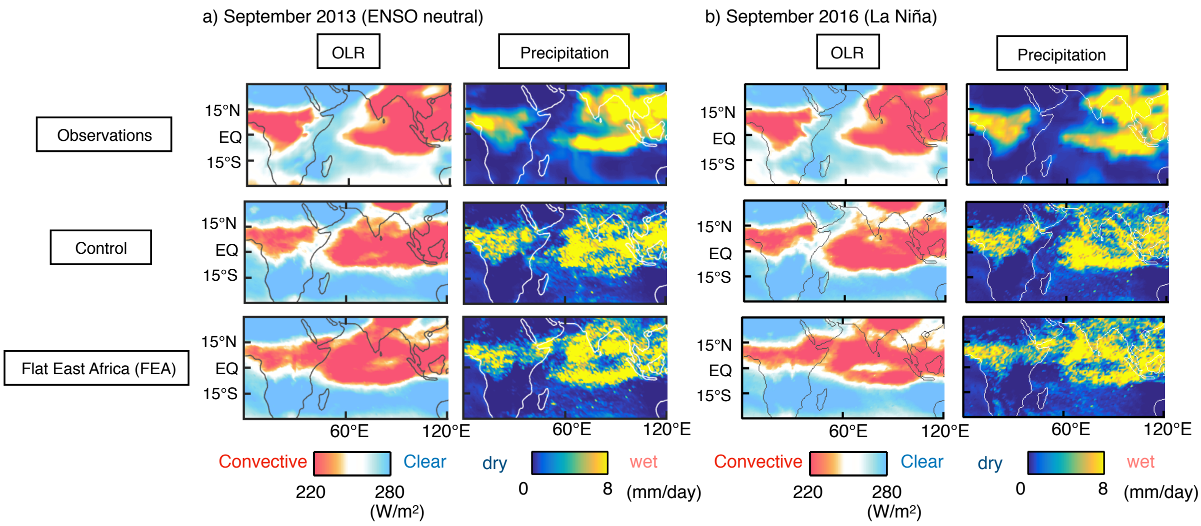


**Figure 8.** (a): As in Fig. 6b, but for OLR (left) and precipitation (right) for 2013. (b): As in (a), but for 2016.

**Figure 1.**

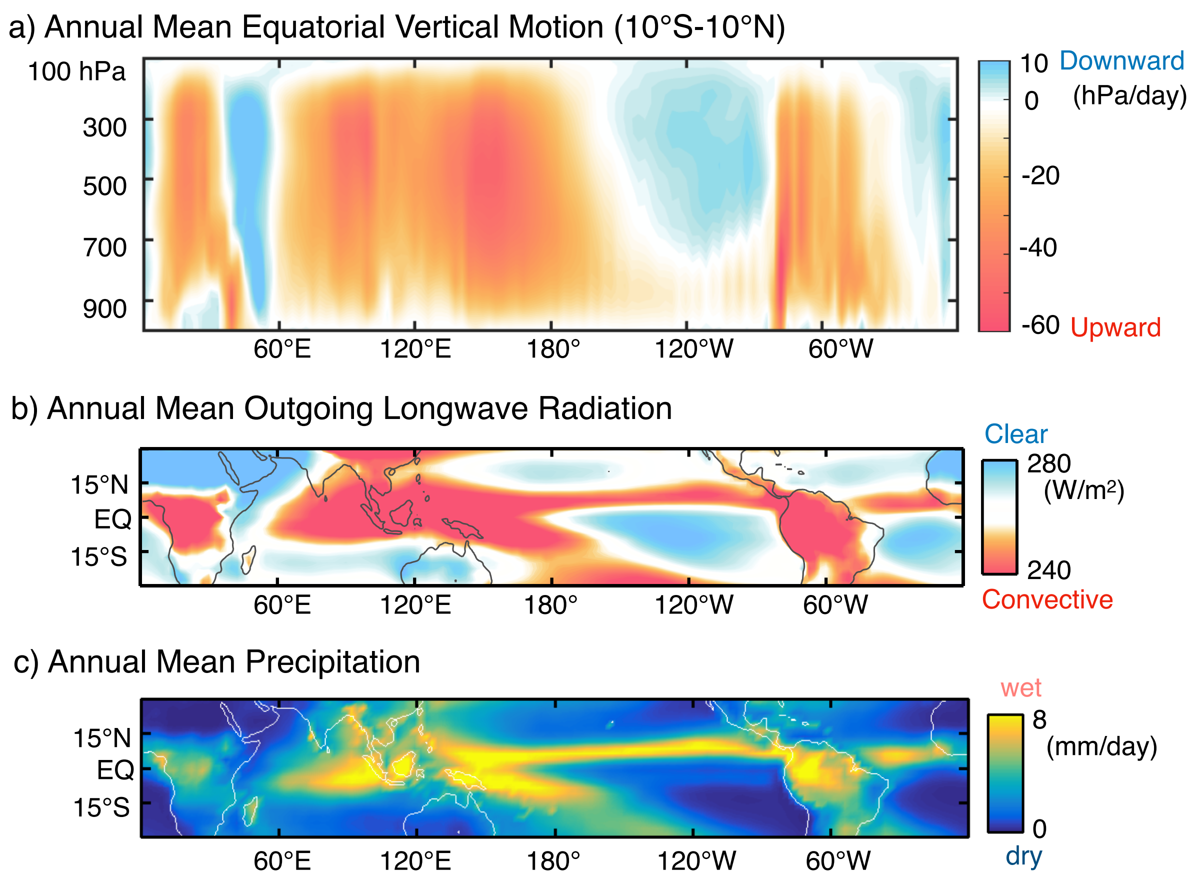
a) Annual Mean Equatorial Vertical Motion (10°S-10°N)
100 hPa
300
500
700
900
60°E
120°E
180°
120°W
60°W
10 Downward
0 (hPa/day)
-20
-40
-60 Upward
b) Annual Mean Outgoing Longwave Radiation
15°N
EQ
15°S
60°E
120°E
180°
120°W
60°W
Clear
280
(W/m2)
240
Convective
c) Annual Mean Precipitation
15°N
EQ
15°S
60°E
120°E
180°
120°W
60°W
wet
8
(mm/day)
0
dry

**Figure 2.**

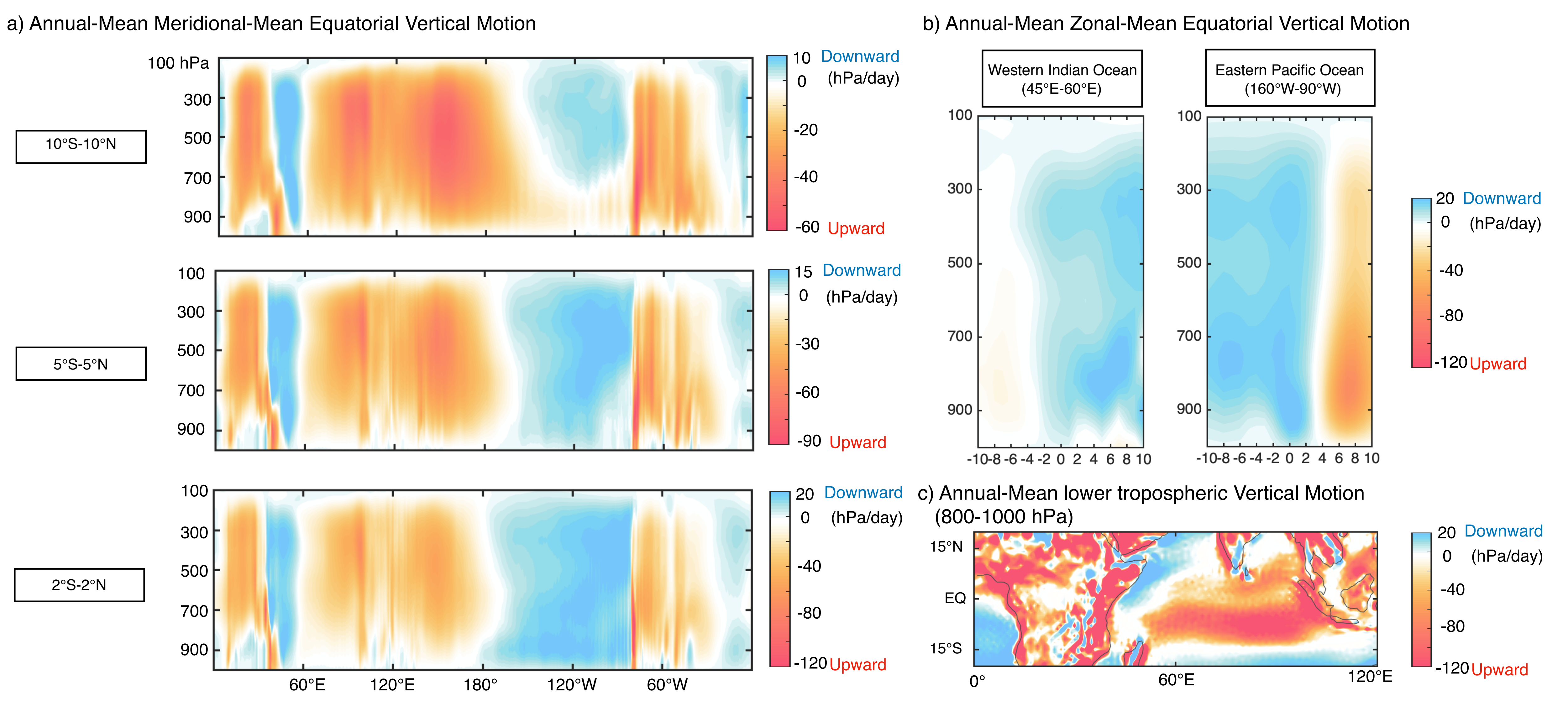

a) Annual-Mean Meridional-Mean Equatorial Vertical Motion
10°S-10°N
5°S-5°N
2°S-2°N
100 hPa
300
500
700
900
60°E
120°E
180°
120°W
60°W
10
0
-20
-40
-60
15
-30
-90
20
-80
-120
Downward
(hPa/day)
Upward
b) Annual-Mean Zonal-Mean Equatorial Vertical Motion
Western Indian Ocean (45°E-60°E)
Eastern Pacific Ocean (160°W-90°W)
-10 -8 -6 -4 -2 0 2 4 6 8 10
c) Annual-Mean lower tropospheric Vertical Motion (800-1000 hPa)
15°N
EQ
15°S
0°
60°E
120°E

**Figure 3.**

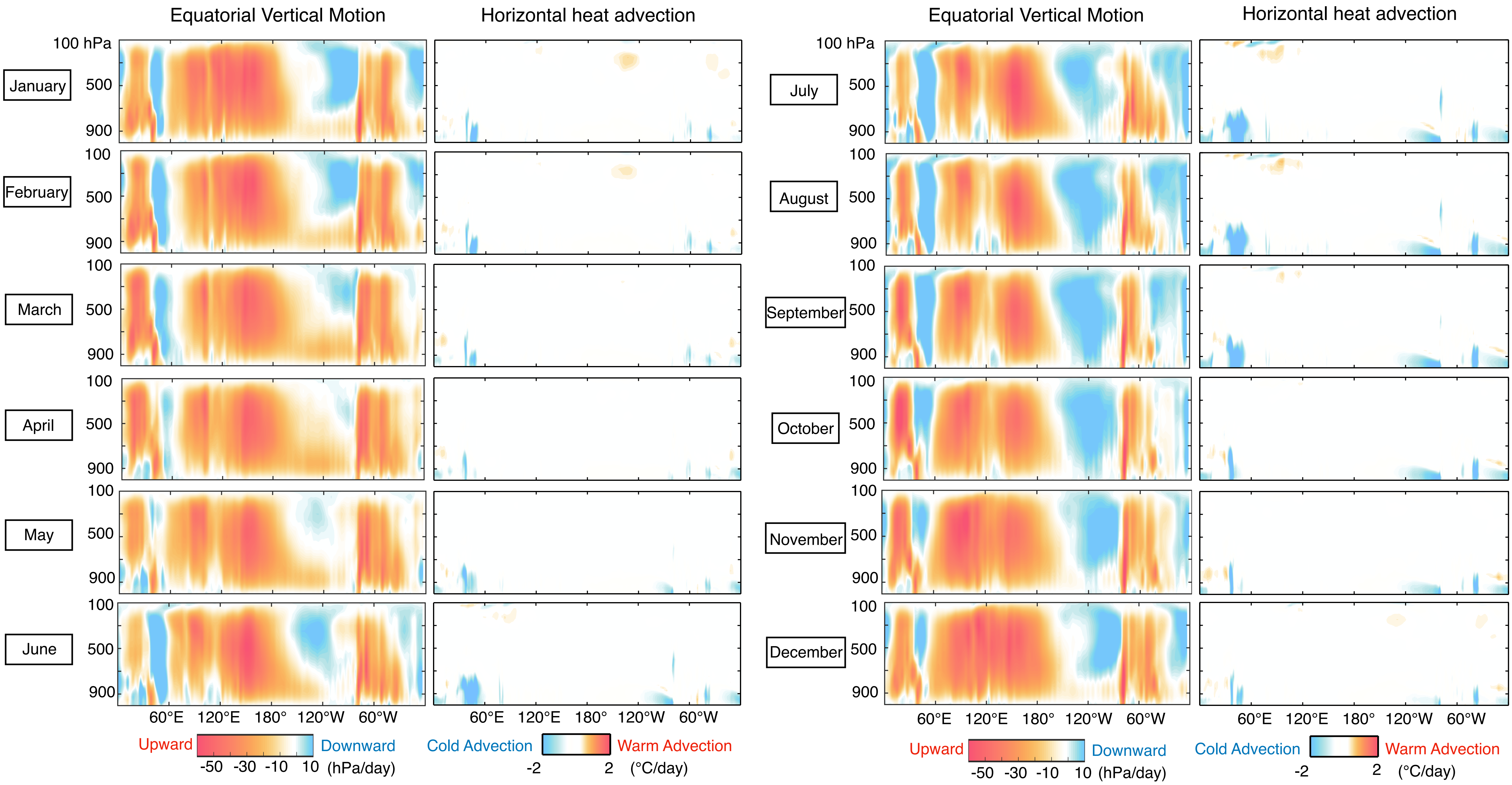

Equatorial Vertical Motion
Horizontal heat advection
Equatorial Vertical Motion
Horizontal heat advection
100 hPa
500
900
January
February
March
April
May
June
July
August
September
October
November
December
60°E 120°E 180° 120°W 60°W
Upward
Downward
-50 -30 -10 10 (hPa/day)
Cold Advection
Warm Advection
-2 2 (°C/day)

**Figure 4.**

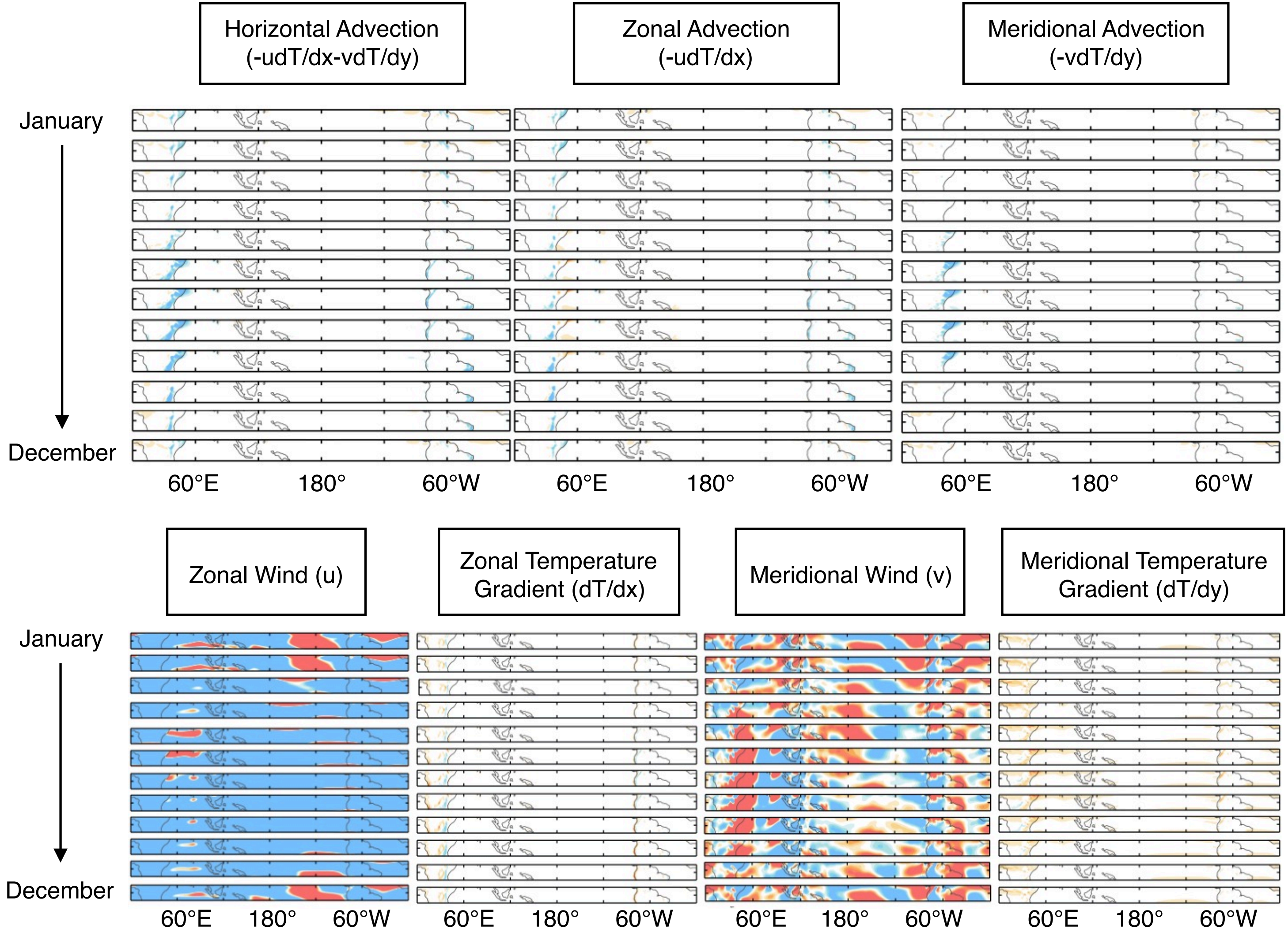
Horizontal Advection (-udT/dx-vdT/dy)
Zonal Advection (-udT/dx)
Meridional Advection (-vdT/dy)
January
December
60°E
180°
60°W
Zonal Wind (u)
Zonal Temperature Gradient (dT/dx)
Meridional Wind (v)
Meridional Temperature Gradient (dT/dy)

**Figure 5.**

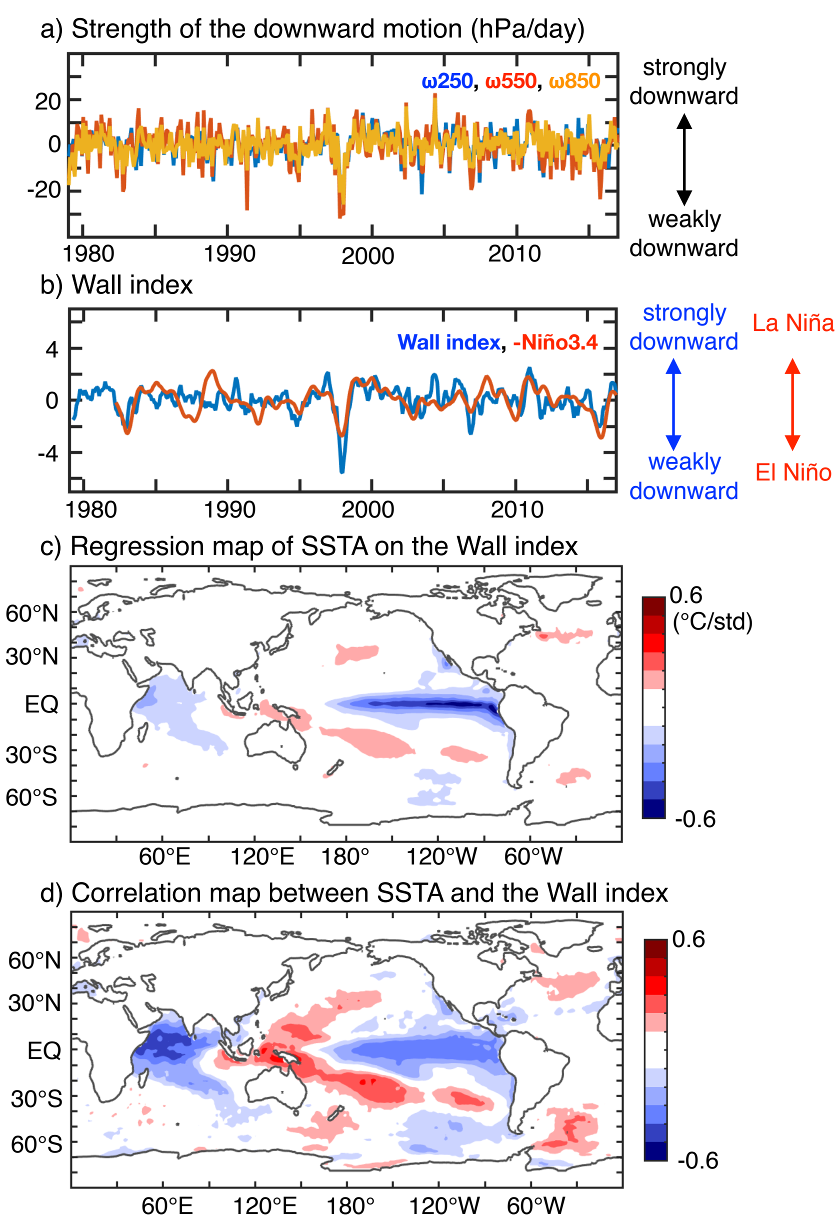

a) Strength of the downward motion (hPa/day)
ω250, ω550, ω850
strongly downward
weakly downward
20
0
-20
1980
1990
2000
2010
b) Wall index
Wall index, -Niño3.4
strongly downward
weakly downward
La Niña
El Niño
4
0
-4
1980
1990
2000
2010
c) Regression map of SSTA on the Wall index
0.6
(°C/std)
-0.6
60°N
30°N
EQ
30°S
60°S
60°E
120°E
180°
120°W
60°W
d) Correlation map between SSTA and the Wall index
0.6
-0.6
60°N
30°N
EQ
30°S
60°S
60°E
120°E
180°
120°W
60°W

**Figure 6.**

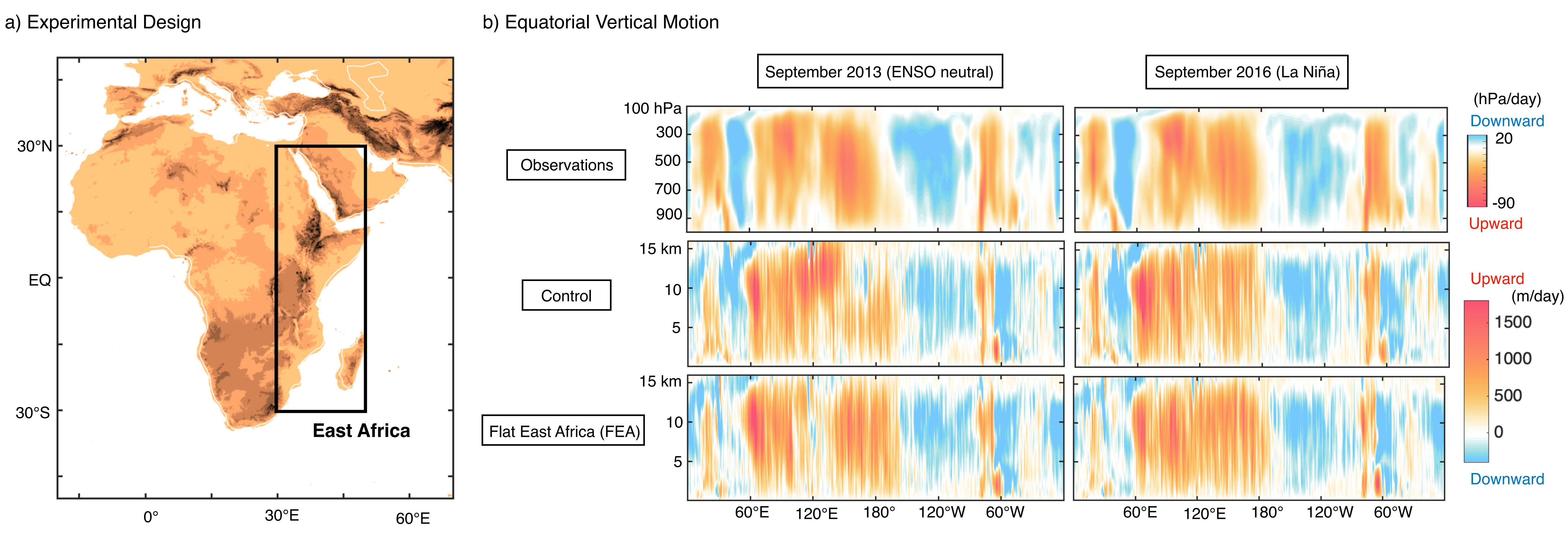

a) Experimental Design
30°N
EQ
30°S
0°
30°E
60°E
East Africa
b) Equatorial Vertical Motion
September 2013 (ENSO neutral)
September 2016 (La Niña)
Observations
Control
Flat East Africa (FEA)
100 hPa
300
500
700
900
15 km
10
5
60°E
120°E
180°
120°W
60°W
(hPa/day)
Downward
20
-90
Upward
(m/day)
1500
1000
500
0

**Figure 7.**

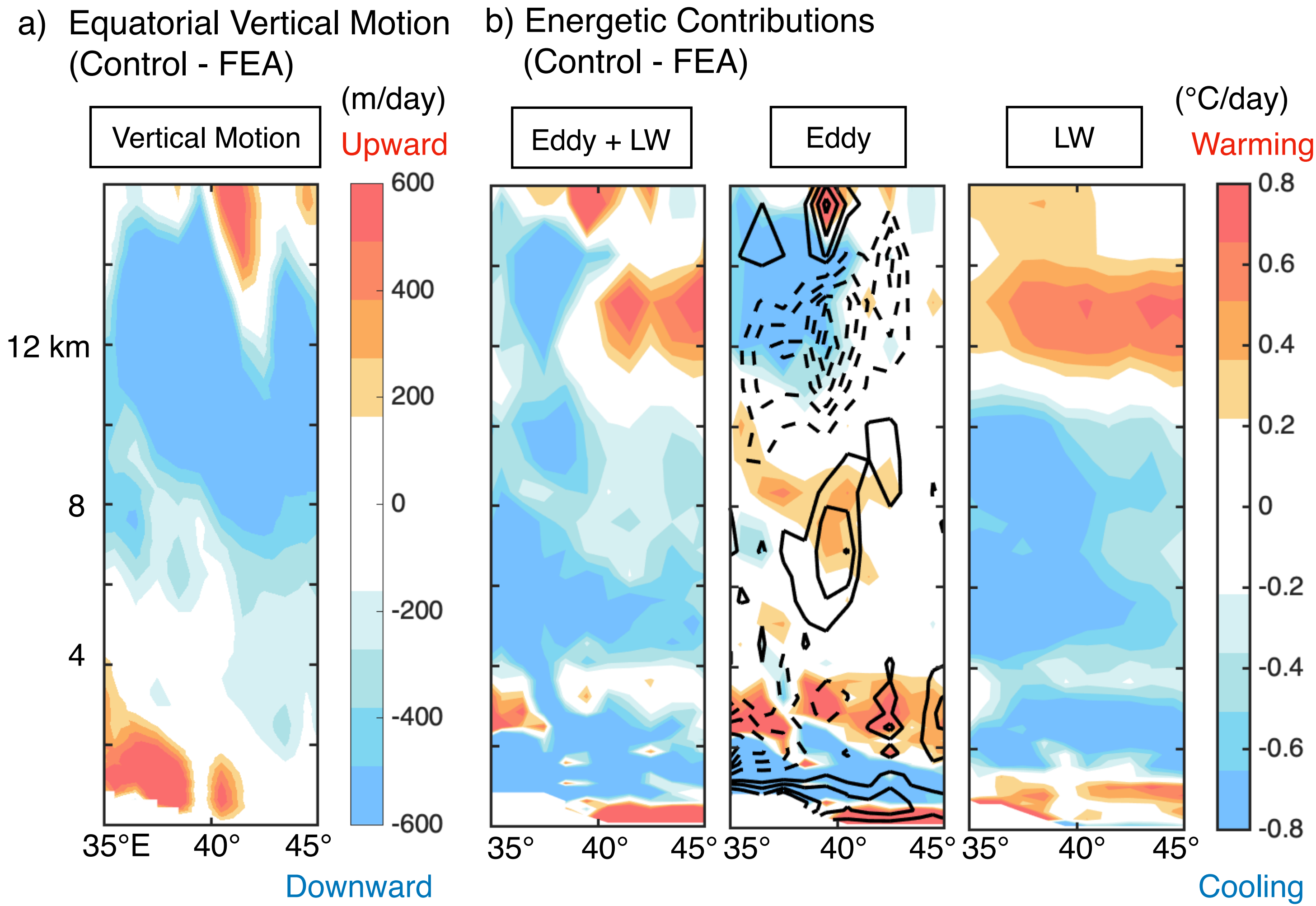
a) Equatorial Vertical Motion
(Control - FEA)
Vertical Motion
(m/day)
Upward
600
400
200
0
-200
-400
-600
Downward
12 km
8
4
35°E
40°
45°
b) Energetic Contributions
(Control - FEA)
Eddy + LW
Eddy
LW
(°C/day)
Warming
0.8
0.6
0.4
0.2
0
-0.2
-0.4
-0.6
-0.8
Cooling
35°
40°
45°

**Figure 8.**

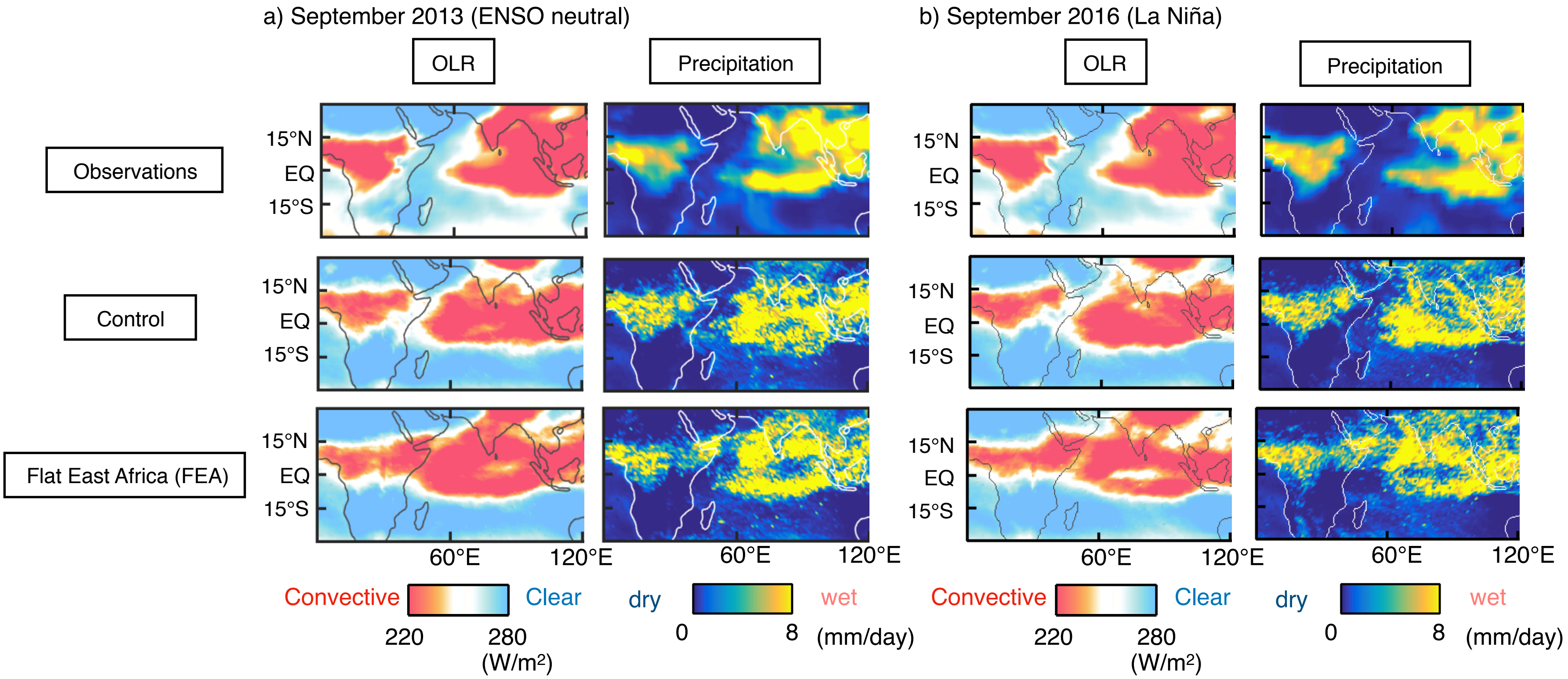
a) September 2013 (ENSO neutral)
b) September 2016 (La Niña)
OLR
Precipitation
OLR
Precipitation
Observations
Control
Flat East Africa (FEA)
15°N
EQ
15°S
60°E
120°E
Convective
Clear
220
280
(W/m2)
dry
wet
0
8
(mm/day)